

Unified formulation of geometrically nonlinear refined beam theories

Original

Unified formulation of geometrically nonlinear refined beam theories / Pagani, A.; Carrera, E.. - In: MECHANICS OF ADVANCED MATERIALS AND STRUCTURES. - ISSN 1537-6494. - STAMPA. - 25:1(2018), pp. 15-31.
[10.1080/15376494.2016.1232458]

Availability:

This version is available at: 11583/2694491 since: 2017-12-11T11:39:12Z

Publisher:

Taylor and Francis Inc.

Published

DOI:10.1080/15376494.2016.1232458

Terms of use:

This article is made available under terms and conditions as specified in the corresponding bibliographic description in the repository

Publisher copyright

(Article begins on next page)

Full-core coupled neutronic/thermal-hydraulic modelling of the EBR-II SHRT-45R transient

*D. Caron, R. Bonifetto, S. Dulla, V. Mascolino,
P. Ravetto, L. Savoldi, D. Valerio, R. Zanino¹*

*NEMO Group, Dipartimento Energia, Politecnico di Torino
Corso Duca degli Abruzzi, 24 - 10129 Torino, Italy*

Abstract

During the last decade the European activities in the field of nuclear fission research include the design of fast reactors cooled by liquid metals. Within this framework, the FRENETIC (Fast REactor NEutronics/Thermal-hydraulicICs) code is being developed at Politecnico di Torino over the last few years. It implements a full-core coupled neutronic/thermal-hydraulic model of a liquid-metal-cooled fast reactor as relevant for two of the six options currently under study within the framework of the Generation-IV International Forum, namely the lead-cooled fast reactors and the sodium-cooled fast reactors. The code validation process involves the participation in a coordinated research project of the International Atomic Energy Agency, aiming at testing different computational tools against the shutdown heat removal tests performed many years ago in the sodium-cooled Experimental Breeder Reactor-II (EBR-II) at Argonne National Laboratory, USA. In this paper, results of the FRENETIC analysis of one of the transients considered in the project, the unprotected EBR-II shutdown heat removal test SHRT-45R, are presented and compared to the measurements, providing the first validation of the coupled neutronic/thermal-hydraulic features of the FRENETIC code.

Keywords: Liquid-metal-cooled fast reactor, EBR-II, multiphysics, coupled neutronics/thermal-hydraulics.

1 Introduction

The research activities in the field of nuclear fission reactors at the international level are strongly focused on innovative reactor designs, such as Generation-IV reactors. For these innovative technologies, the open issues are often characterised by physical features that require the development and/or application of new, multiphysics, integrated simulation tools consisting of accurate models to describe the neutronic and thermal-hydraulic behaviour of the system. Existing multiphysics codes usually include highly simplified models for neutronics and thermal-hydraulics calculations, which may be too simplistic for some design and safety assessments.

To this end, the FRENETIC (Fast REactor NEutronics/Thermal-hydraulicICs) code is under development at Politecnico di Torino for the purpose of the simulation of coupled neutronic/thermal-hydraulic transients in liquid-metal-cooled fast reactors with the core arranged in closed, hexagonal subassemblies [1]. The objective of the code is to provide a description of the coupled neutronic/thermal-hydraulic behaviour of the nuclear reactor core with more refined information with respect to traditional systems codes. A simultaneous objective is to limit the cost in terms of computational effort, which is achieved through an appropriate selection of physical and numerical models.

As regards validation, experimental data is available from sodium-cooled fast reactors, which benefit from a history of development and operation. Within the framework of a coordinated research project (CRP) [2, 3] of the International Atomic Energy Agency (IAEA), some shutdown heat removal tests (SHRTs) of the

¹ Corresponding author: roberto.zanino@polito.it

sodium-cooled Experimental Breeder Reactor-II (EBR-II) at the Argonne National Laboratory (ANL), USA, are being reproduced with the FRENETIC code as a means of validation, through comparison with experimental data and with the results of the other participants to the benchmark activity. This paper focuses on the validation of the FRENETIC code against the unprotected EBR-II shutdown heat removal test SHRT-45R.

2 The FRENETIC code

The FRENETIC code is composed of a neutronic module and a thermal-hydraulic module, which are coupled in order to provide a multiphysics description of a nuclear reactor with hexagonal subassemblies.

The neutronic module of FRENETIC implements the multigroup neutron diffusion equations with delayed neutron precursors [4]

$$\left\{ \begin{array}{l} \frac{1}{v_g} \frac{\partial}{\partial t} \phi_g(\mathbf{r}, t) = \nabla \cdot D_g(\mathbf{r}, t) \nabla \phi_g(\mathbf{r}, t) - \Sigma_{tg}(\mathbf{r}, t) \phi_g(\mathbf{r}, t) + \\ \quad + \sum_{g'=1}^G \Sigma_{sgg'}(\mathbf{r}, t) \phi_{g'}(\mathbf{r}, t) + (1 - \beta) \chi_{pg}(\mathbf{r}, t) \sum_{g'=1}^G v \Sigma_{fg'}(\mathbf{r}, t) \phi_{g'}(\mathbf{r}, t) + \\ \quad + \sum_{i=1}^R \chi_{dgi}(\mathbf{r}, t) c_i(\mathbf{r}, t) + S_g(\mathbf{r}, t), \quad g = 1, \dots, G, \\ \frac{\partial}{\partial t} c_i(\mathbf{r}, t) = \beta_i \sum_{g'=1}^G v \Sigma_{fg'}(\mathbf{r}, t) \phi_{g'}(\mathbf{r}, t) - \lambda_i c_i(\mathbf{r}, t), \quad i = 1, \dots, R, \end{array} \right. \quad (1)$$

where $\phi_g(\mathbf{r}, t)$ is the flux of neutron energy group g of a total G neutron energy groups, $c_i(\mathbf{r}, t)$ is the density of delayed neutron precursor family i of a total R delayed neutron precursor families, v_g is the velocity, $D_g(\mathbf{r}, t)$ is the diffusion constant, $\Sigma_{tg}(\mathbf{r}, t)$ is the macroscopic cross section for total reactions, $\Sigma_{sgg'}(\mathbf{r}, t)$ is the macroscopic cross section for scattering reactions from neutron energy group g' to neutron energy group g , $v \Sigma_{fg'}(\mathbf{r}, t)$ is the macroscopic cross section for fission neutron production in neutron energy group g' , $\chi_{pg}(\mathbf{r}, t)$ is the prompt neutron fission energy spectrum, $\chi_{dgi}(\mathbf{r}, t)$ is the delayed neutron fission energy spectrum due to precursor family i , β_i is the fraction of delayed neutrons produced in fission appearing in precursor family i ($\beta = \sum_{i=1}^R \beta_i$) and λ_i is the decay constant of precursor family i . In the absence of external sources ($S_g(\mathbf{r}, t) = 0, \forall g$), Eqs. (1) are modified by dividing the macroscopic cross section for fission neutron production by the effective multiplication eigenvalue, k_{eff} .

These equations are solved by means of a nodal discretisation in space [5] and a quasi-static discretisation in time [6]. The macroscopic cross sections characterising the materials present in each homogeneous node are functions of time, either explicitly due to the variation in time of the materials themselves or implicitly due to the variation in time of the temperature of the materials.

The thermal-hydraulic module solves the time-dependent mass, momentum and energy conservation laws for the fuel and the coolant in each subassembly [1]. For the coolant (subscript c), the full set of conservation equations are considered [7]

$$\begin{cases} \frac{D}{Dt} \rho_c(\mathbf{r}, t) = -\rho_c(\mathbf{r}, t) \nabla \cdot \mathbf{u}(\mathbf{r}, t) \\ \rho_c(\mathbf{r}, t) \frac{D}{Dt} \mathbf{u}(\mathbf{r}, t) = \nabla \cdot \hat{\boldsymbol{\sigma}}(\mathbf{r}, t) + \rho_c(\mathbf{r}, t) \mathbf{f}(\mathbf{r}, t) \\ \rho_c(\mathbf{r}, t) \frac{D}{Dt} e_c(\mathbf{r}, t) = \hat{\boldsymbol{\sigma}}(\mathbf{r}, t) : \nabla \mathbf{u}(\mathbf{r}, t) - \nabla \cdot \mathbf{q}_c(\mathbf{r}, t) + Q_c(\mathbf{r}, t) \end{cases} \quad (2)$$

where $\rho_c(\mathbf{r}, t)$ is the mass density, $\mathbf{u}(\mathbf{r}, t)$ is the velocity of the coolant and $e_c(\mathbf{r}, t)$ is the internal energy per unit mass, $\hat{\boldsymbol{\sigma}}(\mathbf{r}, t)$ is the stress tensor of the coolant, $\mathbf{f}(\mathbf{r}, t)$ is the applied external force per unit mass of the coolant, $\mathbf{q}_c(\mathbf{r}, t)$ is the conduction heat flux and $Q_c(\mathbf{r}, t)$ is the external heat source per unit volume, which includes heat transfer effects between the fuel and the coolant as well as between the channel walls and the coolant. The differential operator D/Dt denotes the classical Lagrangian derivative.

Under the hypothesis of immobile structures, the fuel (subscript f) is described by the heat conduction equation

$$\rho_f(\mathbf{r}, t) \frac{\partial}{\partial t} e_f(\mathbf{r}, t) = -\nabla \cdot \mathbf{q}_f(\mathbf{r}, t) + Q_f(\mathbf{r}, t) \quad (3)$$

where $\rho_f(\mathbf{r}, t)$ is the mass density, $e_f(\mathbf{r}, t)$ is the internal energy per unit mass, $\mathbf{q}_f(\mathbf{r}, t)$ is the conduction heat flux and $Q_f(\mathbf{r}, t)$ is the external source of thermal energy per unit time per unit volume, which includes heat transfer effects between the fuel and the coolant in addition to energy production due to fission. The system of equations (2) is closed by assuming that the fluid obeys the hypotheses of Navier-Stokes and both Eqs. (2) and (3) make use of the Fourier hypothesis, with the assistance of the standard thermodynamic relations.

With the inclusion of appropriate heat transfer correlations, as well as relationships for the relevant thermophysical properties of the materials under consideration, Eq. (2) in one-dimensional form (along the channel axis) and Eq. (3) are solved simultaneously for a given channel by the finite element method in space and the theta method in time. As a result, a single, average value of the fuel and coolant temperatures, coolant velocity and pressure is computed at each axial node of each channel. The individual one-dimensional channels are then thermally coupled to their adjacent neighbours in the two-dimensional horizontal plane, resulting in a three-dimensional, full-core model. In transient conditions, the inter-channel coupling is explicit with respect to the time.

The physical models presented allow to describe the coupled neutronic/thermal-hydraulic behaviour of the reactor core. Each model is rendered complete by imposing proper initial and boundary conditions, the specifics of which depend on the problem under consideration.

The coupling between the two modules is achieved by providing the spatial distribution of the fuel and coolant temperatures as output from the thermal-hydraulic module and input to the neutronic module while the spatial distribution of the power density is output from the neutronic module and input to the thermal-hydraulic module. As each module may operate on a different computational domain and/or computational mesh, further elaboration of the distributions by the receiving module is typically required. In the neutronic module, the received fuel and coolant temperatures are spatially averaged on the volume of the computational node and attributed to the entire homogeneous volume. In the thermal-hydraulic module, the received linear power distribution is localised in the volume of the fuel pin.

With the auxiliary of an appropriate temperature-dependent model for the macroscopic cross sections, this approach to the coupling allows to account for the relevant feedback effects on each of the neutronic and the thermal-hydraulic models; that is, on the macroscopic cross sections in the neutronic equations and on the heat source term due to fission in the thermal-hydraulic equations. In the cross section model implemented in FRENETIC, each macroscopic cross section for each reaction in each energy group of each homogeneous

material is assumed to be characterised by two state variables, the fuel temperature T_f and the coolant temperature T_c , resulting in a temperature-dependence of the form $\Sigma_{xg}^m(T_f, T_c)$ for reaction x in group g of homogeneous material m . In order to preserve generality, the temperature dependence may be read in tabular form, in which case the appropriate value of the macroscopic cross section for a given material is obtained through bivariate linear interpolation with respect to the fuel and the coolant temperatures that characterise the computational volume in which the material is present. Thus, the number of discrete evaluations of the macroscopic cross section that are necessary to properly describe its temperature dependence, as well as the manner in which the temperature dependence is generated, are both left as modelling parameters.

The algorithm according to which the coupling is performed differs between steady-state and transient analyses, as seen in Figure 1. In steady-state computations, the steady-state neutronics equations (obtained by setting all derivatives with respect to time equal to zero in Eqs. (1)) and the steady-state thermal-hydraulics equations (obtained by setting all derivatives with respect to time equal to zero in Eqs. (2) and (3)) are solved in series using a fixed-point iteration until tolerances imposed on the variation of the power distribution and the variation of the temperature distribution between successive iterations are simultaneously satisfied. In transient computations, the two sets of equations are solved in parallel and at each time step selected for the coupling, the power and the temperature distributions are simply exchanged without iteration, resulting in a coupling scheme which is explicit in time.

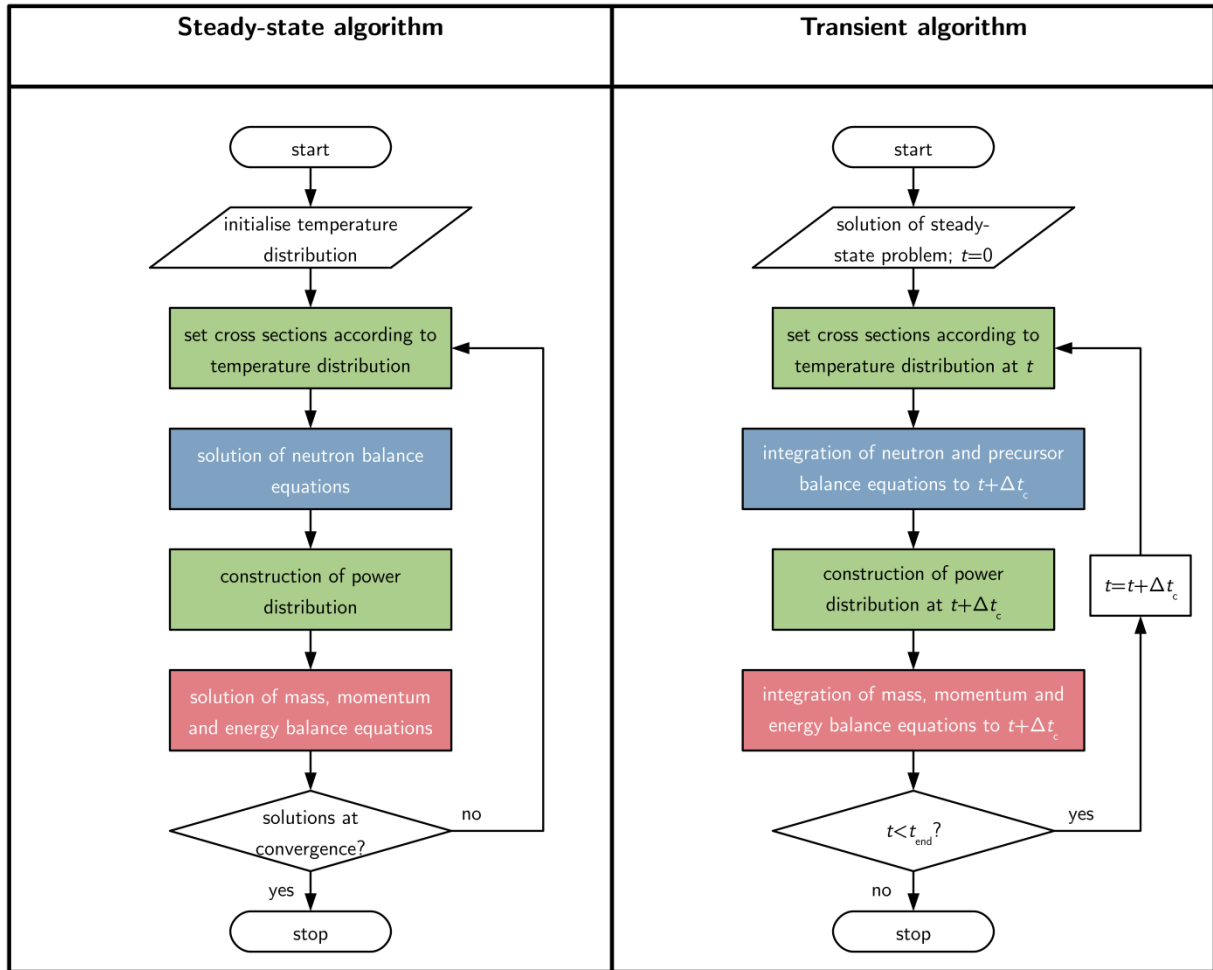


Figure 1. FRENETIC solution algorithms: steady-state (left) and transient (right). Operations in blue are those of the neutronic module; operations in red are those of the thermal-hydraulic module; operations in green involve the coupling of the two modules; Δt_c is the time step for the coupling of the neutronic and the thermal-hydraulic solutions.

Throughout the course of the development of the code, each module has been individually verified against numerical test calculations. Furthermore, the physical models of the thermal-hydraulic module have been already validated on experimental data in both single-subassembly [8] and multiple-subassembly [9] configurations. The present work presents the results of the first validation activity of the coupled neutronic/thermal-hydraulic features of the integral code.

3 The EBR-II reactor and the SHRT-45R transient

The EBR-II is a sodium-cooled fast spectrum reactor, formerly in operation at ANL-West from 1964 to 1994 [10]. The core design is of hexagonal geometry, nominally consisting of 637 hexagonal subassemblies, of which the 127 located in the inner seven rings comprise the driver core. The total fissile inventory is approximately 229 kg of uranium-235 and 5 kg of plutonium (all isotopes), fabricated into a unique uranium-metallic fuel and producing a nominal power of 62.5 MW thermal, 20 MW electric. As seen in Figure 2, the primary system is in pool configuration, consisting of a primary coolant inventory of 286 t of sodium, and the heat transport system adopts the standard three-loop configuration. Further technical details are available in [10, 11, 12].

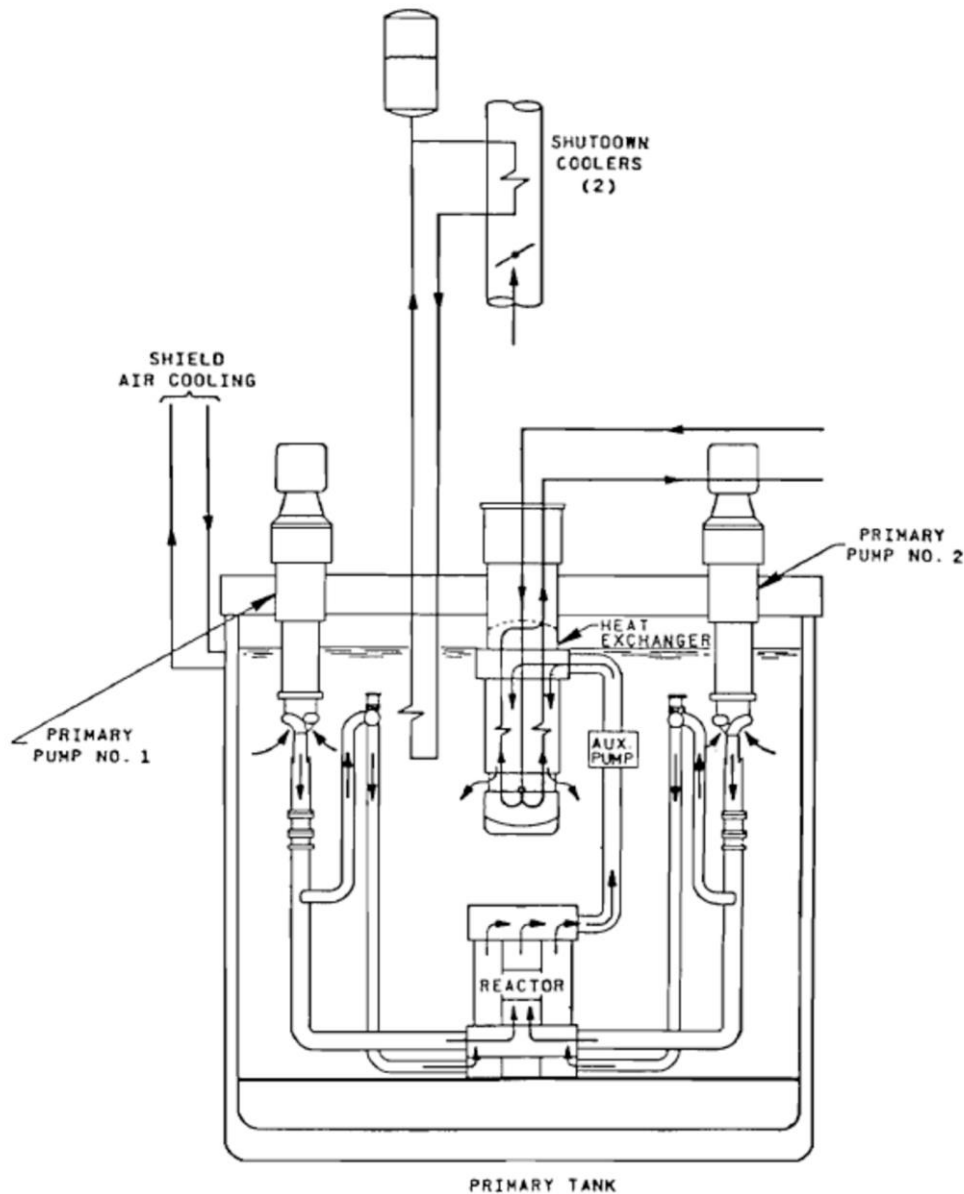


Figure 2. EBR-II primary system configuration [11].

Operation of the EBR-II sought to support the demonstration of the closed nuclear fuel cycle [11]. During its lifetime, the EBR-II served several purposes, including but not limited to: the demonstration of the closed nuclear fuel cycle, the study of advanced fuels through irradiation experiments and the demonstration of the inherent, passive safety features of liquid-metal-cooled fast reactors. With reference to the latter, the SHRTs, conducted from 1984 to 1986, consist of both protected and unprotected transients. In addition to demonstrating the inherent passive safety features of the reactor design, the SHRT programme had as an objective to provide experimental data for the validation of computer codes that could be used in the design and licensing of liquid-metal-cooled fast reactors.

One particular SHRT, the SHRT-45R, conducted on 3 April 1986, replicated an unprotected loss of flow scenario by the simultaneous trip of the primary and the intermediate coolant pumps of the reactor while operating at nominal conditions, accompanied by the intentional disabling of the plant protection system [11]. As a consequence of the pump trip, the coolant flow rate decreased and both the fuel and coolant temperatures within the reactor rose. In response, the inherent feedback mechanisms led to an insertion of negative reactivity that ultimately brought the reactor to a subcritical state. The experimental results of this test have been adopted as a benchmark in the framework of the IAEA CRP.

Participants of the CRP have been requested to compute the core multiplication factor, the effective delayed neutron fraction, the spatial distribution of the subassembly power, the temporal evolution of the integral power, reactivity coefficients, as well as temperatures, pressures and flow rates in numerous locations of the primary system for the transient. Several experimental measurements of these quantities are available to participants for comparison, while other evaluations have been proposed to perform code-to-code comparison. As regards those quantities relevant to the reactor core, hence the part of the system considered by FRENETIC, the temporal evolution of the reactor-integrated power due to fission events and the temporal evolution of the coolant temperatures and mass flow rates at multiple axial positions of two instrumented subassemblies are available.

4 FRENETIC model of the EBR-II and the SHRT-45R

The approaches to the modelling of the neutronics and the thermal-hydraulics aspects of the EBR-II reactor and the SHRT-45R transient are now described. The benchmark specifications provide design drawings, nominal operating parameters and irradiated fuel compositions [11, 12]; from these data, the neutronic and the thermal-hydraulic models are developed. As described previously, the FRENETIC code models the reactor core; hence, all other parts of the primary, secondary and tertiary circuits are not modelled directly. For reference, the core layout of the EBR-II for the SHRT-45R is shown in Figure 3, from which it is evident that the configuration of the core of the reactor is characterised by a high degree of heterogeneity in terms of the different types of subassemblies present. This characteristic impacts certain aspects of the modelling, as described in this section.

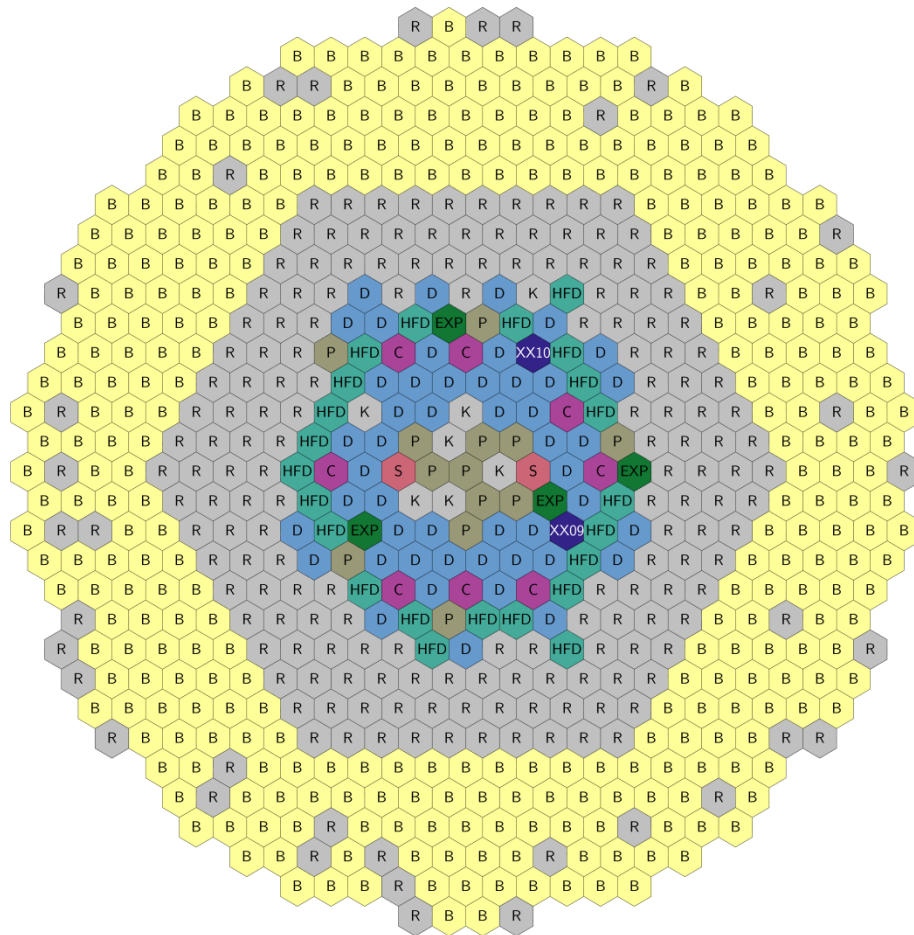


Figure 3. EBR-II core layout for the SHRT-45R transient. D: driver subassembly; HFD: high flow driver subassembly; P: partial driver subassembly; B: blanket subassembly; R: reflector subassembly; C: control subassembly; S: safety

subassembly; K: stainless steel dummy subassembly; EXP: experimental facility (N.B. geometries differ among different occurrences); XX##: instrumented subassembly.

4.1 Neutronic model

The neutronic model comprises the generation of a library of temperature-dependent macroscopic cross sections for use in the nodal diffusion solver, as well as the definition of the nodal model. The heterogeneity of the reactor poses a significant challenge in the determination of the homogenised, few-group cross sections required by a core solver.

The macroscopic cross sections are generated in this work following a procedure that is summarised graphically in Figure 4. Starting from the detailed geometrical specifications and the isotopic compositions of the relevant materials (first column of Figure 4), an equivalent axial-symmetric cylindrical model of the reactor is defined, consisting of six radial regions and up to five axial regions of homogenised materials (second column of Figure 4). These regions are defined in order to group subassemblies of similar geometry and composition, while attempting to preserve their positions (in a polar-integrated sense) relative to the axis of the cylinder. A steady-state neutronic analysis of the cylindrical model of the reactor is then performed using the Serpent Monte Carlo code [13] and the JEFF-3.1.1 cross section library [14, 15]. On the basis of the observed flux spectrum and considering also previous approaches to the few-group modelling of other sodium-cooled fast spectrum systems [16], the six-group energy structure defined in Table 1 is selected to generate the multigroup cross sections. Similarly, the standard eight families of delayed neutron precursors are used in the generation of the delayed neutron data.

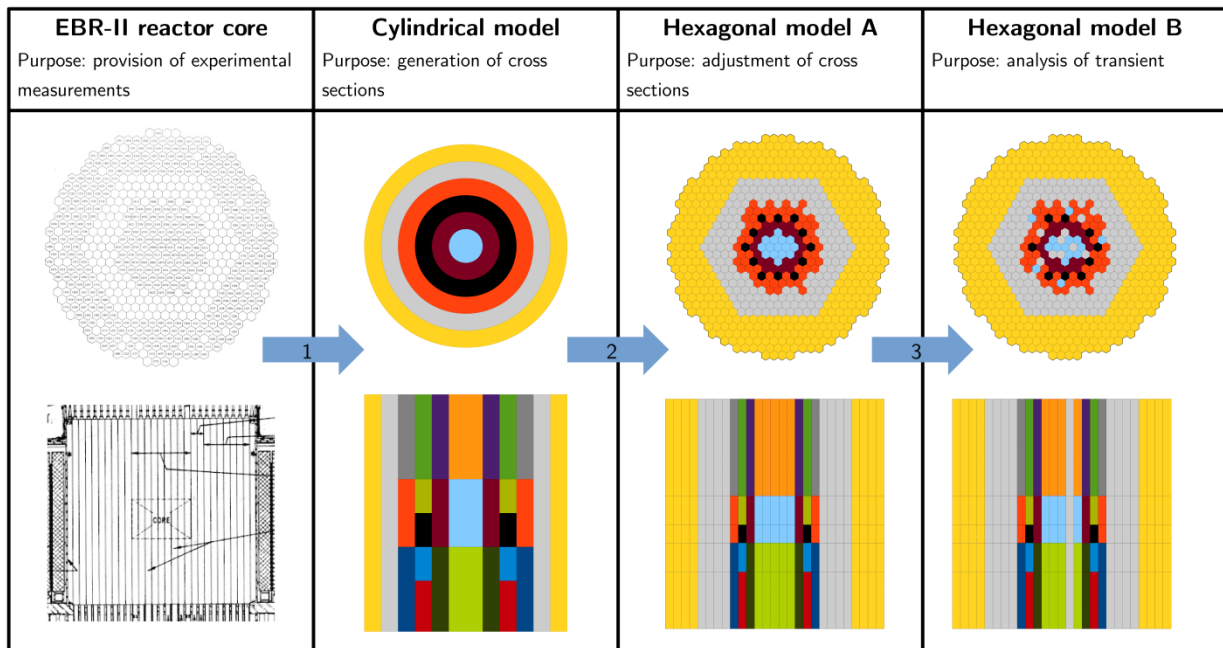


Figure 4. Approach to EBR-II neutronics modelling. From the left, first column: true geometry from the benchmark specifications [11]; second column: cylindrical geometry adopted for the Monte Carlo calculation and the generation of cross sections; third column: nodalisation of the whole core and localisation of materials for the criticality calculation; fourth column: modification of the cross sections to better represent the heterogeneity. Different colors represent unique, heterogeneous materials. Schematics not to scale.

The aforementioned procedure describes the process by which the macroscopic cross sections are generated for one configuration of the reactor under a specified set of operating conditions. In order to obtain a library of macroscopic cross sections which depend on the temperature, the process is repeated at different configurations of the system. As the SHRT-45R transient does not foresee the (intentional) movement of any of the core structures, this process reduces to the evaluation of the same materials at different temperatures.

In particular, the temperatures of the materials which comprise the fuel and the temperatures of fuel materials which comprise the coolant are independently varied (although each is maintained spatially uniform throughout the reactor); when necessary, the temperatures of the structural materials are approximated by applying an appropriate average of the surrounding materials. This process of varying the temperatures accounts for thermal feedback due to the Doppler effect (by enabling the appropriate option passed to the cross section processing module in the input to the Serpent code) as well as the coolant density effects (by explicitly recalculating the coolant density according to an appropriate approximation formula [17] and modifying the input to the Serpent code). This approach does not account for the geometric deformation and corresponding density effects of the structural materials.

The temperature values of 400 K, 700 K and 1000 K are selected for both the fuel and the coolant in this evaluation. The two limit values, 400 K and 1000 K, enclose with some margin the range of temperatures encountered during the transient, while the intermediate value, 700 K, is arbitrarily selected at the midpoint of the two bounds in order to examine the linearity of the variation of the macroscopic cross sections as a function of the temperature. In fact, as the linearity is verified for the present set of macroscopic cross sections, the evaluation at additional points on the temperature axes is omitted.

Having obtained the macroscopic cross sections from the Serpent code, the nodal model is then defined. The hexagonal geometry of the subassemblies constituting the reactor core is defined in the FRENETIC code. Each subassembly is homogenous and is assigned the material of the cylindrical zone to which it belonged in the Monte Carlo cylindrical model. Axially, the mesh is imposed so as to allow the same homogeneous regions as those defined in the Monte Carlo cylindrical model (third column of Figure 4).

Depending on the definition of the groups of subassemblies for the concentric cylindrical regions, the return to the hexagonal configuration from the cylindrical configuration has the potential to incorrectly localise material which is either insufficiently or excessively fissile with respect to the reality. When this occurs, a more appropriate material is substituted (fourth column of Figure 4) and, after all substitutions are complete, in order to account for no longer having preserved the materials present between the true reactor and the nodal model, the global set of macroscopic cross sections is then adjusted by applying a set of correction factors. The correction factors are applied individually to each macroscopic cross section of each energy group of each homogeneous material in order to preserve the reaction rate density in the region in which a substitution occurs.

In the nodal model, a computational node consists of one hexagonal prism. Hence, no additional subdivision in the xy -plane occurs. The axial regions, preliminarily defined to accommodate the correct placement of the homogenised materials, are further subdivided as necessary so that each computational node is approximately between 10.0 cm and 13.5 cm in height. This is in comparison to the 5.8929 cm lattice pitch in the xy -plane. The boundary conditions of zero incoming partial current are imposed on all external surfaces of the reactor. For the neutronic computations of the flux shape, a convergence criterion of 10^{-5} is imposed on the relative error of the neutron flux.

Although it is anticipated that the role of decay heat is not to be neglected, this analysis disregards the phenomenon. Comprehensive and reliable nuclear data characterising the decay heat generated in fast spectrum systems are not yet available, rendering it difficult to accurately describe the system under analysis. Although it may be suggested to employ the decay heat data currently used in thermal reactors, neglecting completely the decay heat phenomenon (by assuming that all energy generated in fission is released immediately) is justified inasmuch as it provides a limit value.

4.2 Thermal-hydraulic model

The thermal-hydraulic model requires the definition of the geometry of the various subassemblies present in the reactor, as well as the definition of the time-dependent boundary conditions.

All coolant channels are modelled. As suggested by the core layout presented in Figure 3, a total of twelve typologies of subassemblies are considered. From the point of view of thermal-hydraulics, the various subassemblies differ in terms of geometry and materials composition; namely the dimensions of the duct, the possible presence of a concentric annulus in which coolant flows (referred to as the thimble) and the number, dimension and material of the pins. Representative geometries of the two instrumented subassemblies are shown in Figure 5. Save for the presence of instrumentation and the disposition of the pins containing fissile material, in the region occupied by the pins, the transverse section of the instrumented subassembly XX09 is similar to that of the partial driver, driver and high-flow driver subassemblies. In the axial direction, the domain modelled by the thermal-hydraulic module is limited to the region occupied by the fuel pins, which is delimited in Figure 6.

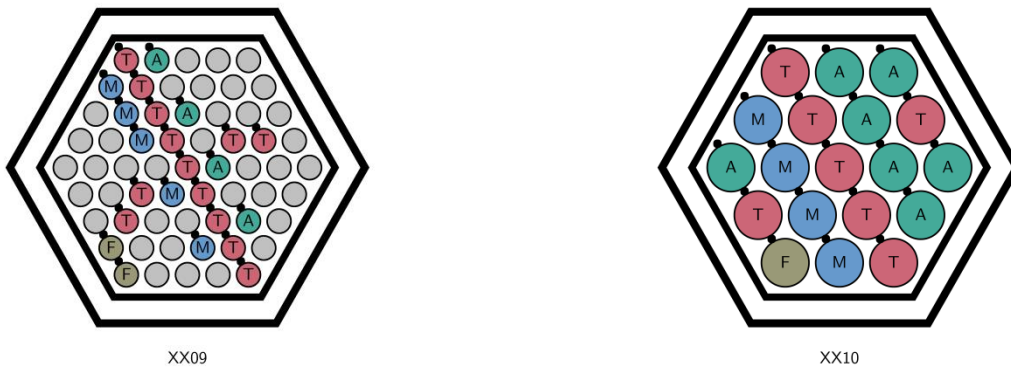


Figure 5. Geometry of instrumented subassemblies XX09 and XX10; for locations of subassemblies in the core, see Figure 3, and for axial locations of thermocouples, see Figure 6. F: flowmeter, M: mid-core thermocouple group, T: top-core thermocouple group, A: above-core thermocouple group.

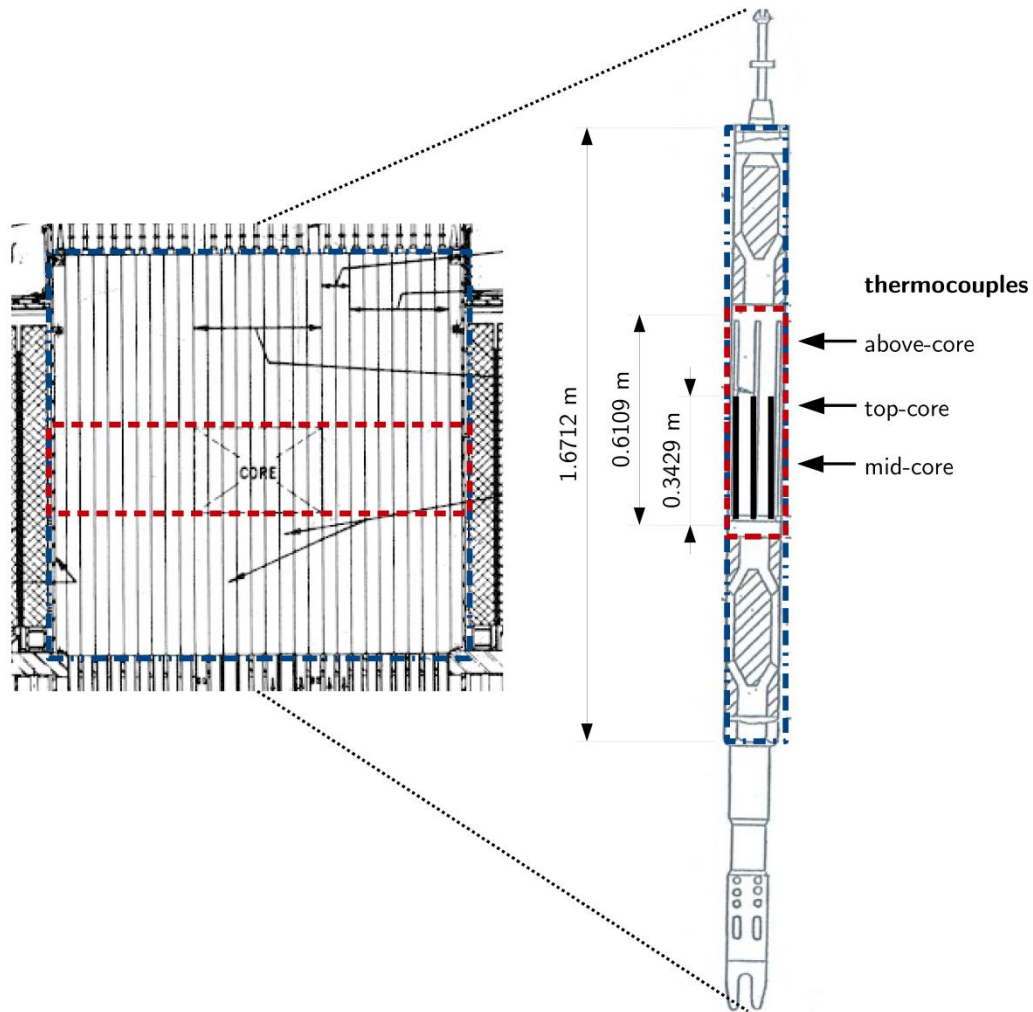


Figure 6. Axial domain of the EBR-II modelled in the analysis. Superimposed on the schematics [11], the dashed-dotted blue line identifies the domain considered by the neutronic module while the dashed red line identifies the domain considered by the thermal-hydraulic module (the pin region). Also indicated are the axial positions of the three thermocouple groups (see Figure 5) as well as the dimensions of the subassembly height, the total pin length and the pin active region.

Thermophysical properties for the fissium fuel are provided in the benchmark specifications [11], while those for the sodium coolant are obtained from an appropriate reference [17]. The heat transfer coefficient between the fuel and the coolant is obtained from the correlation used by Westinghouse [7].

The necessary set of boundary conditions for the thermal-hydraulic module of FRENETIC is obtained through the elaboration of the available data, describing both the nominal operating conditions as well as the experimental measurements. The spatial distribution of the inlet mass flow rates in stationary conditions are obtained from computations made by ANL during the planning phase of the test using the EBRFLOW code [11]. Data for the flow rate in the thimbles of the relevant channels are derived by forcing the thimble-to-total ratio of the mass flow rates to match the experimental values of the two instrumented channels. Inlet coolant temperatures for both the inner channel and the thimble are set equal to the temperature of the coolant in the inlet plenum, which is available as an experimentally measured quantity.

In transient conditions, the spatial distribution of the inlet mass flow rates is maintained equal to the steady-state value, while the total flow rate is scaled according to an amplitude factor coming from the measured

data of the second of the two primary pumps (the data recording of the first being disabled). That is, the mass flow rate of channel (or thimble) k at time t is written as $\dot{m}_k(t) = A(t)\dot{m}_k(0)$, with $A(t)$ the relative mass flow rate of the entire core and $\dot{m}_k(0)$ the steady-state value of the mass flow rate in channel (or thimble) k . This model is justified by the fact that, in the transient, all coolant pumps are simultaneously tripped. Similarly, the inlet coolant temperatures $T_{in}(t)$ are measured throughout the transient and used as boundary conditions.

The radial mesh on which the solution is computed within the pins varies approximately between 0.015 cm and 0.10 cm, depending on the dimensions of the pin itself. The axial mesh is uniform with a characteristic dimension of approximately 0.51 cm. A convergence criterion of 10^{-4} is imposed on the relative error of the temperatures.

5 Results

A series of coupled neutronic/thermal-hydraulic computations is performed with the FRENETIC code. The first set of results pertains to the steady-state analysis, which establishes the initial conditions of the subsequent transient analysis. In steady-state conditions, the tolerances employed in the fixed-point iterations to determine the power distribution and the temperature distributions of the coupled solution (see Figure 1) are one order of magnitude less than the values used in the individual solvers for the flux and the temperatures, respectively.

5.1 Steady-state results

According to the model described previously, the computed value of the effective multiplication eigenvalue is 0.97619, which is within 2400 pcm of the expected value of 1 for a critical system in steady-state conditions. The computed value of the effective delayed neutron fraction is 728 pcm, redistributed among the eight families of delayed neutron precursors as shown in Table 2. The effective neutron lifetime is determined to be $2.795 \cdot 10^{-7}$ s.

The steady-state distribution of the axially-integrated subassembly power is shown in Figure 7 for the subassemblies present in the inner seven rings of the EBR-II reactor. Although no experimental data against which to compare the computed values is available, the benchmark specifications do provide the spatial distribution of the subassembly power in steady-state conditions computed with the discrete ordinates transport code DOT-III [18]. The full set of modelling assumptions is not discussed in the reference; however, it is known that the code can solve problems in two-dimensional geometry and that both neutron and photon fluxes were computed, with the resulting power distribution comprising both effects [11]. Consequently, the values reported in the benchmark specifications do not allow a direct comparison, but they do provide a point of reference upon which to assess some of the later results which do in fact involve a comparison with experimental measurements. In particular, those subassemblies for which zero power is reported are due to the assumption of the FRENETIC code that the only source energy production is that due to fission events; that is, the neutron kerma term and the photon kerma term are neglected, the latter of which is due to the lack of a photon transport model in the code. At a local, subassembly level, especially when considered in relative terms, the effect appears drastic in those subassemblies which do not contain fissile material and, consequently, do not generate any power in the FRENETIC model, although in absolute terms the effect may not be so great, as in fact the greatest contributions to the generation of power originate from fission. This effect can be observed in all the other subassemblies of the reactor, since the total power of the system is imposed and therefore, compared to the true situation, more power comes to be generated in those subassemblies containing fissile material.

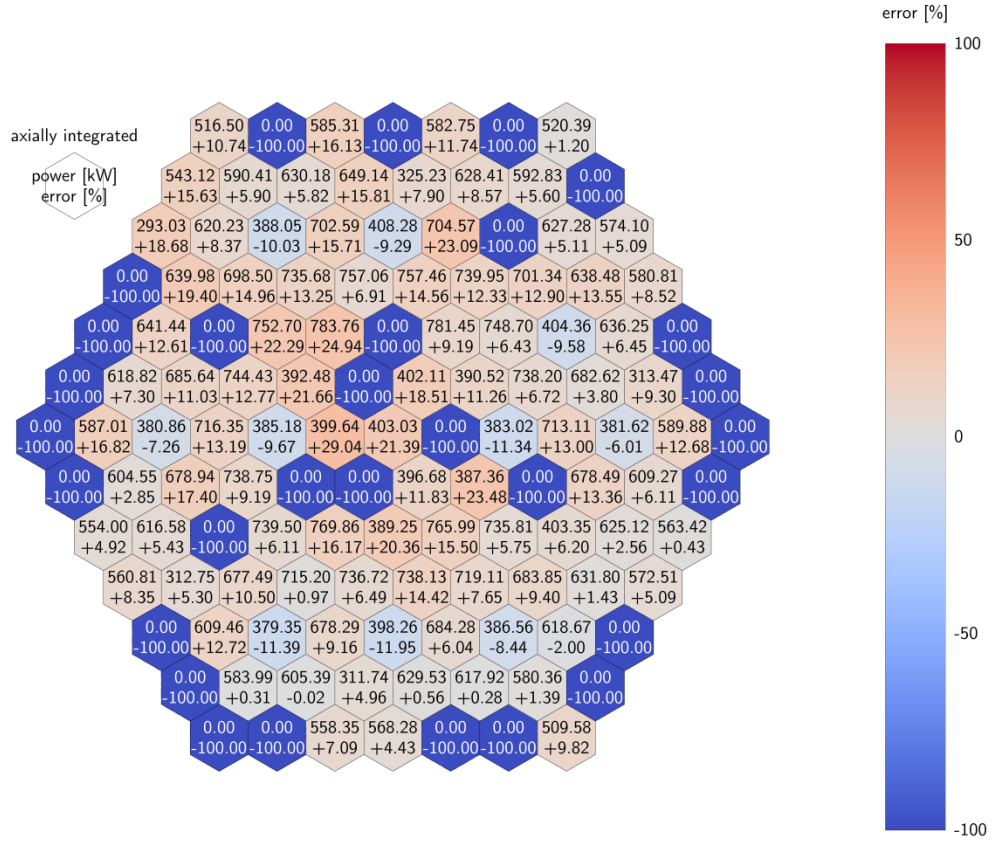


Figure 7. Axially-integrated subassembly power, together with relative error with respect to values reported in the benchmark specifications, of the inner seven rings of the EBR-II in steady-state conditions.

Considering the same inner seven rings of the EBR-II reactor, information regarding the distribution of peak fuel centreline and peak coolant temperatures in steady-state conditions is reported in Figure 8.

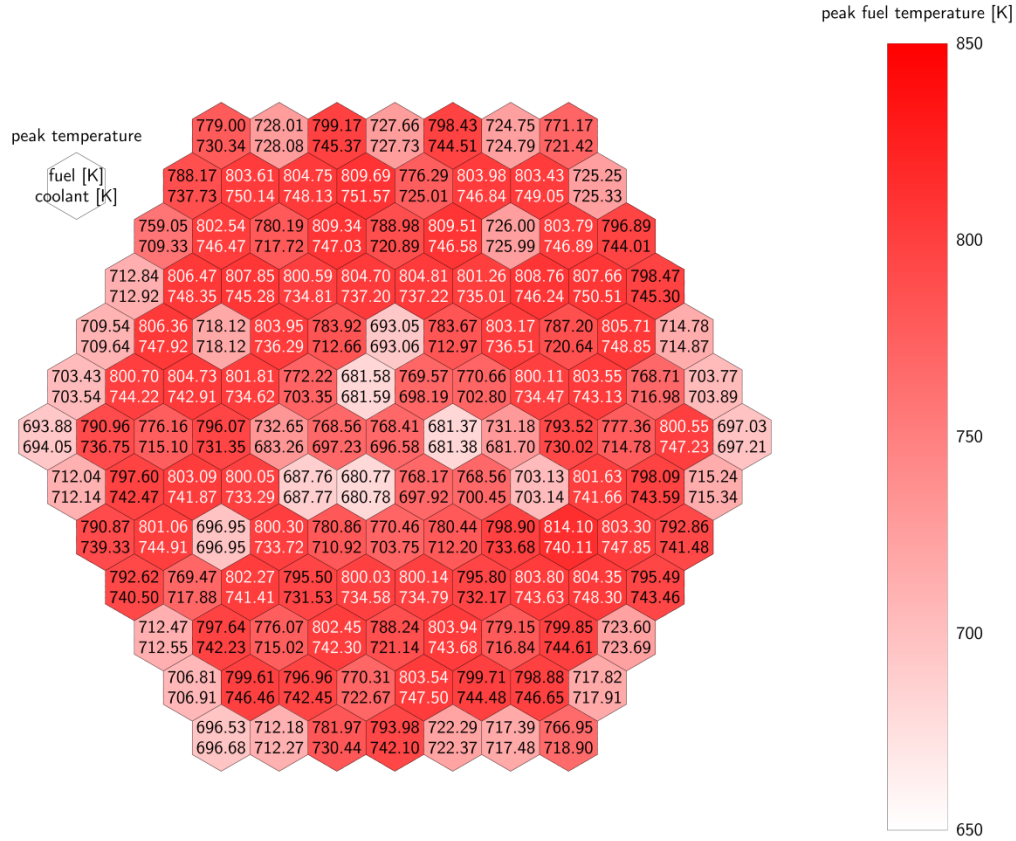


Figure 8. Distribution of peak (centreline) fuel temperature and coolant temperature in the inner seven rings of the EBR-II in steady-state conditions.

In Figure 9, the steady-state axial distribution of the computed coolant temperature in the two instrumented subassemblies XX09 and XX10 (see Figure 3) is presented and compared with the measurements. A direct comparison between the computed value and the measurement is not possible, as the thermocouples are located at different positions in the xy -plane while the value computed by the FRENETIC code is an average value for the transverse section of the channel. To this end, the experimental data are depicted as a band spanning between the minimum and the maximum temperatures measured by the group of thermocouples at the specified axial location (see Figure 5 and Figure 6), in which it is understood that an accurately computed value will be located within this band. In Figure 9, only the part of the axial domain occupied by the fuel pins and included in the thermal-hydraulic model is shown.

The comparison between computed results and measurements for the XX09 subassembly is satisfactory: this subassembly contains fissile material, hence the temperature increases as the fluid moves along the length of the subassembly in the fuel region. The different trend that can be observed in the lower and upper part of the active region of the pin (0-0.2 m vs. 0.2-0.34 m) is due to the homogenisation process, which places materials with different fissile properties in these two axial regions. The fact that the fluid arrives at the bottom of the subassembly already partially heated (about 655 K with respect to the inlet temperature of approximately 617 K) is also due to the homogenisation process, as some fissile material is placed below that level. The active height of the fuel pin stops at approximately 0.34 m, see again Figure 6; thereafter, the slight temperature decrease is due to the heat transfer to neighbouring subassemblies at lower temperatures.

The comparison between computed results and measurements for the XX10 subassembly is less favourable: this subassembly contains no fissile material and, as already explained above, the photon heat deposition is

not modelled; consequently, no heat source term is present and the subassembly is heated only by the adjacent subassemblies. Consequently, the XX10 subassembly is colder and the neighbouring subassemblies are hotter than in the reality, explaining the trend of the computed axial profile, which progresses from under-estimation to over-estimation with respect to the experimental measurements as the fluid moves along the length of the subassembly.

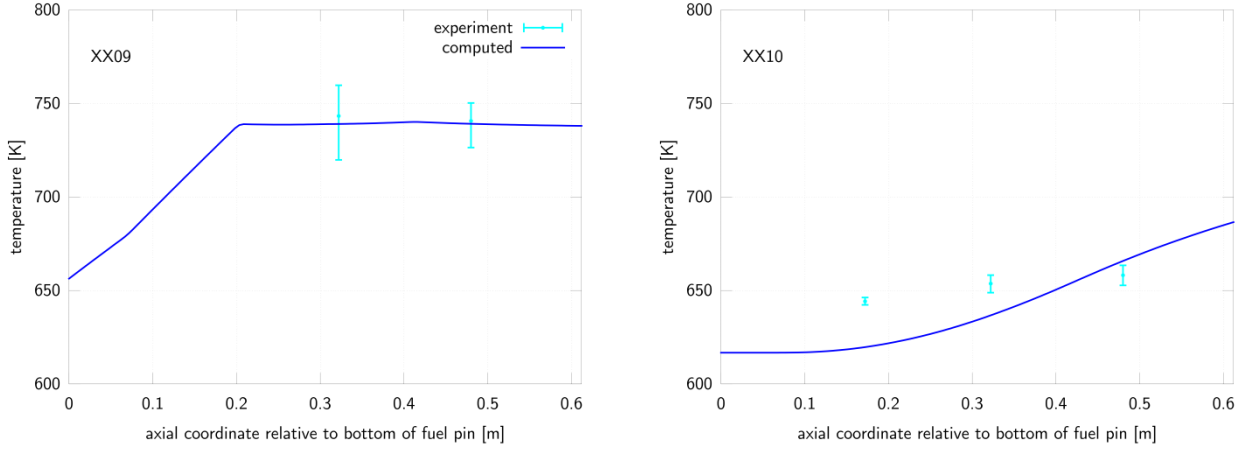


Figure 9. Steady-state coolant temperature in instrumented subassemblies XX09 (left) and XX10 (right); for locations of subassemblies, see Figure 3, and for locations of thermocouples, see Figure 5 and Figure 6. The experimental band covers the values between the minimum and the maximum temperatures measured at the specified axial location.

5.2 Transient results

The first 300 s of the SHRT-45R transient are analysed with FRENETIC. Due to the nature of the transient, in particular, as the initiating event is the loss of coolant flow to all pumps providing coolant to the reactor, only the amplitude of the flux is foreseen to vary while the shape remains more or less constant; consequently, it is expected that the point-kinetics method is sufficient for the temporal integration scheme of the neutronics equations. First, this hypothesis is confirmed by comparing a subset of the results obtained using a quasi-static method to those obtained with the point-kinetics method for a short time interval. After demonstrating that the point-kinetic approach is sufficient for this transient, the simulation is conducted to 300 s and a larger set of results are analysed. In all cases, the integration of the thermal-hydraulic equations is effected with a time step of $5 \cdot 10^{-3}$ s, which is also employed as the coupling time step of the two modules.

As a reference case, the neutronics equations are integrated according to the predictor-corrector quasi-static method, using a shape time-step and a reactivity time-step both equal to 10^{-3} s; the convergence criterion on the neutron flux, when recomputed at the end of each shape time step, is the same as that imposed for the steady-state conditions (a relative error of 10^{-5}). In order to assess the necessity of the quasi-static method, a comparison of these results is made to those obtained with the point-kinetic method using the same reactivity time step and maintaining unvaried the parameters used to discretise the thermal-hydraulic equations and those relative to the coupling of the neutronic and thermal-hydraulic solutions. Representative results for some integral parameters computed using the quasi-static method and the point-kinetic method are presented in Table 3. As anticipated by the foregoing discussion, the results are the same within the imposed accuracy, thereby justifying the use of the point-kinetic method in order to analyse the transient on longer time scales.

The evolution of the total power, both experimental and computed, is shown in Figure 10 along with the accompanying evolution of the computed net reactivity. Some discrepancy is expected due to both the absence of neutron and photon kermas, as described previously, as well as the fact that the FRENETIC model neglects decay heat. The disagreement between the measured and the computed values for the fission power at the beginning of the transient is due to neglecting decay heat entirely in the model. This is confirmed by the fact that the relative error between the two values is +6.8 %, which is of the same order of

magnitude as the decay-to-total power ratio in steady-state conditions (for thermal reactors) [7]. Correspondingly, as the model assumes that all power resulting from fission is released promptly, more heat is deposited early in the transient than with respect to the real situation, ultimately leading to stronger feedback effects that act to decrease the power level at a rate faster than in reality. The fact that the computed power is in good agreement with the experimentally measured value for times less than approximately 100 s and then begins to slightly deviate for longer times indicates that the models implemented in the FRENETIC code adequately describe the physical phenomena which are dominant on the short term but not those which are dominant on the long term. This effect may be related to the absence of a model for the thermal expansion of the core structures, as this effect is overshadowed by the Doppler effect during the first 100 s, when the temperatures are changing rapidly, but not thereafter. An additional consideration regards the decay heat, since the prolonged presence of a source of thermal energy would contribute to increased temperatures and to additional feedback effects.

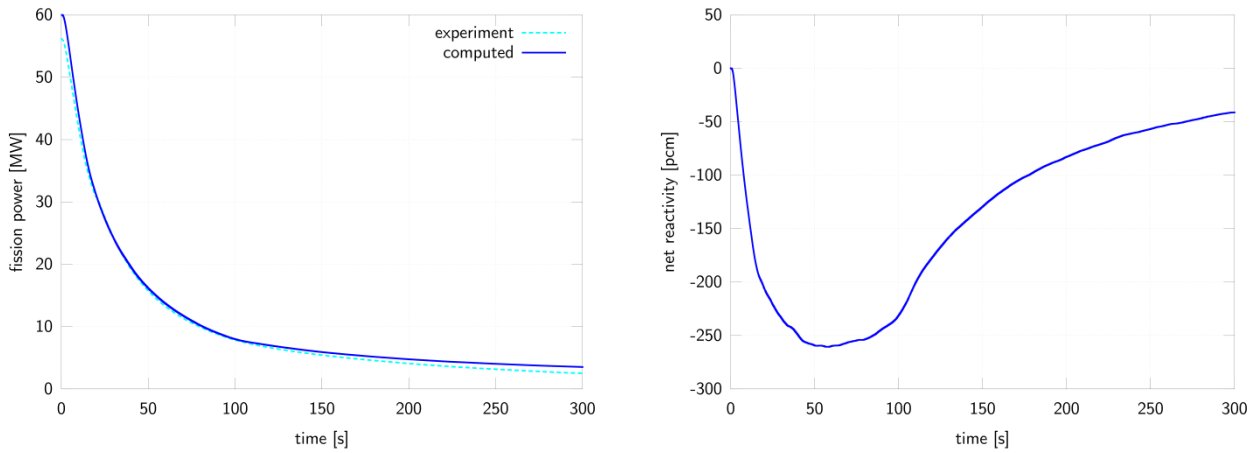


Figure 10. Temporal evolution of the total power (left) and the net reactivity (right).

The evolution of the peak temperature at the fuel centreline, at the fuel surface and in the coolant is shown in Figure 11. As foreseen in the experiment analysis, the temperatures rise but remain within an acceptable margin of safety limits (sodium vaporisation in atmospheric conditions occurs at $1154.7 \text{ K} \pm 1.3 \text{ K}$ [17], while the melting temperature of the fissium fuel onset begins at approximately 1283 K and concludes at approximately 1373 K [19, 20]). As anticipated from the physics aspects which are modelled, peak temperatures occur in correspondence to the maximum feedback reactivity.

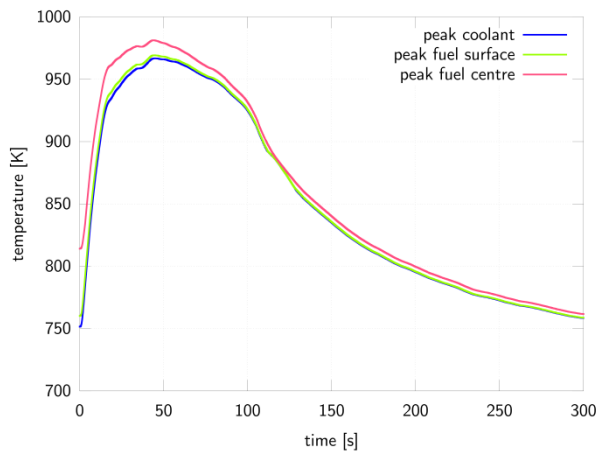


Figure 11. Computed peak temperature evolution at the fuel centreline, at the fuel surface and in the coolant.

The evolution of the coolant temperature at selected axial locations of the instrumented subassemblies is shown in Figure 12 and Figure 13. In these figures, the experimental values are depicted as a band spanning between two temperature values, which correspond to the minimum and the maximum temperatures measured in the subassembly at the specified axial location.

In the XX09 instrumented subassembly, Figure 12, for both of the available thermocouples, it is observed that the computed result remains within the experimental band for the first 25 seconds, underestimating the peak value which is measured at around 50 seconds. Thereafter, the computed result follows a similar trend as the measurement, although underestimating the value by about 25 K-50 K.

In the XX10 instrumented subassembly, Figure 13, a different behaviour is observed depending on the axial location. As regards the mid-core thermocouple, while the computed result follows the trend of the experimental measurement, the correct value is underestimated by approximately 25 K. Instead, at the top-core and above-core thermocouples, the peak value experiences an overestimation that increases as the axial position increases. However, the experimental measurement is reproduced with an error within ± 10 K after approximately 125 seconds.

In both cases, the differences between simulation and measurements can be explained on the basis of the previous discussions. The presence of neutron and photon keramas would change the distribution of the power at a given point in time, influencing the heat source term in each subassembly as well as changing the heat transfer among adjacent subassemblies, ultimately influencing the distribution of the temperature at that point in time. Consequently, local feedback effects would be either stronger or weaker as appropriate, thereby contributing to a different behaviour of the neutron flux, thus the power and the temperature, at successive points in time. Similarly, the inclusion of decay heat in the model would change, at a global level, the time-dependent behaviour of the temperature, as the power generated in fission would arrive with a time delay rather than immediately, which is expected to affect the location of the peak temperature (which appears too early, as seen both in Figure 12 and in Figure 13) as well as its maximum value.

Moreover, the assumptions on the mass flow rate used as boundary condition play a non-negligible role in the temperature calculation: the hypothesis that both pumps behave exactly in the same way during the trip and that the mass flow rate distribution in the core is constant during the whole transient can affect the temperature estimation in a stronger way as time goes by, but unfortunately no additional data are available to make better assumptions [9].

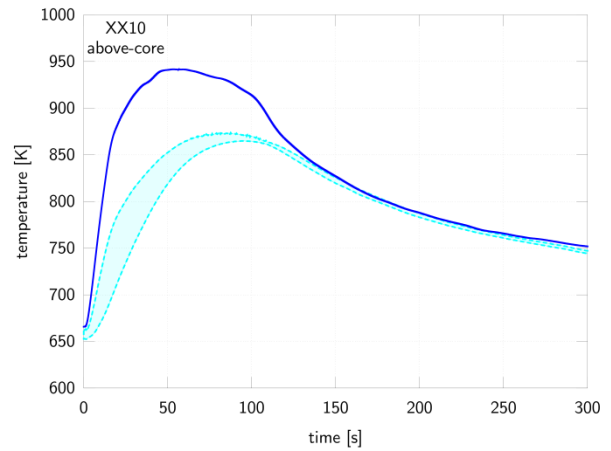
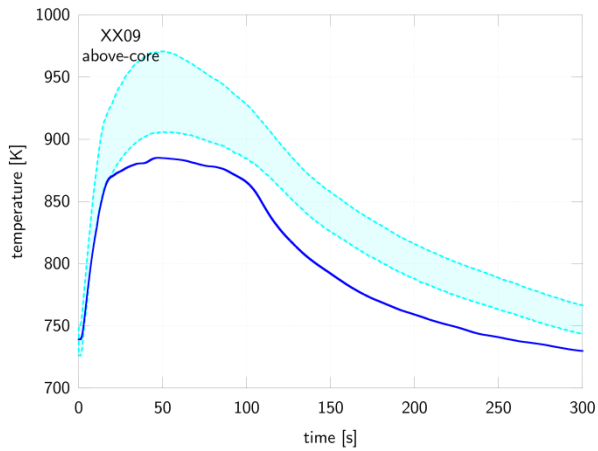
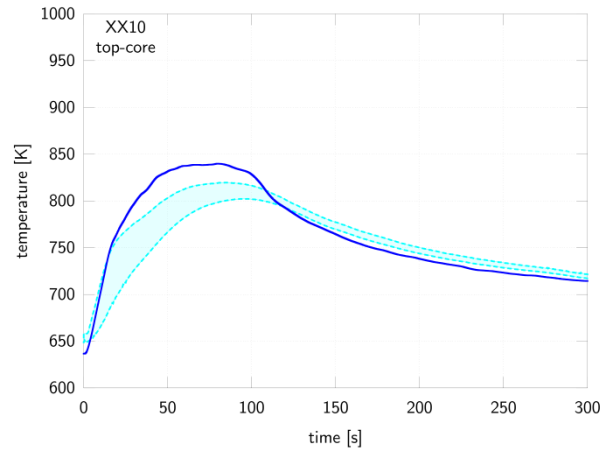
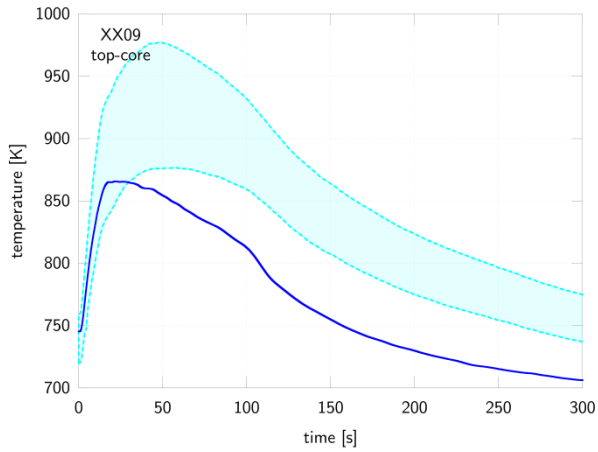
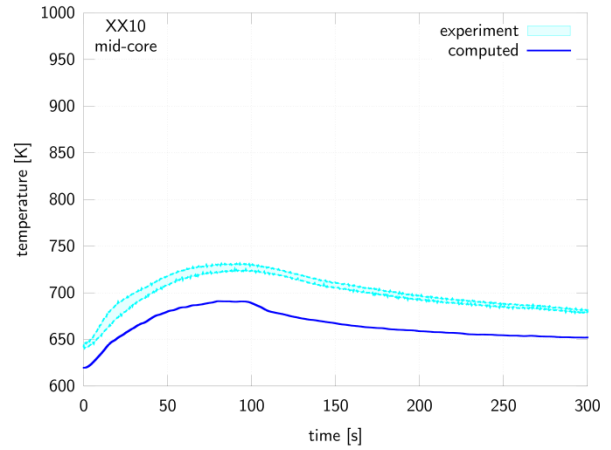
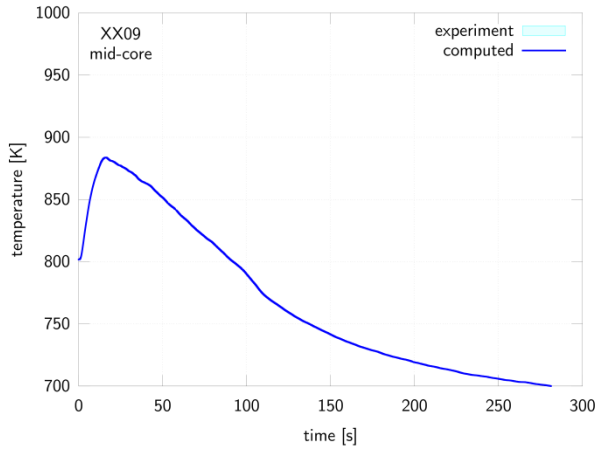


Figure 12. Temporal evolution of the coolant temperature at multiple axial positions of the XX09 instrumented subassembly (for locations, see Figure 3 and Figure 5 and Figure 6). The experimental band covers the values between the minimum and the maximum temperatures measured at the specified axial location. No experimental data are available for the mid-core position as those thermocouples were disabled during the transient.

Figure 13. Temporal evolution of the coolant temperature at multiple axial positions of the XX10 instrumented subassembly (for locations, see Figure 3 and Figure 5 and Figure 6). The experimental band covers the values between the minimum and the maximum temperatures measured at the specified axial location.

Some supplementary information regarding the axial distribution of the temperatures and the heat source term due to fission in the XX09 instrumented subassembly is shown in Figure 14. As the transient progresses, the axial distribution of the temperature changes as a result of the various physical phenomena involved. Early in the transient, while the heat source term is relatively elevated and the coolant flow rate remains close to its nominal value, the spatial distribution of the temperatures is similar to that observed in steady-state conditions. As the transient progresses, notwithstanding that the heat source term decreases in

magnitude, the coolant flow rate slows down resulting in an increased transit time. Consequently, the coolant acquires more energy, which is then transported downstream, causing an additional temperature increase in the plenum area of the fuel pins above the active height of the core. As in Figure 12, the experimental measurement is captured in the first 25 seconds of the transient; thereafter, the computed result consistently underestimates the experimental measurement by 25 K-50 K.

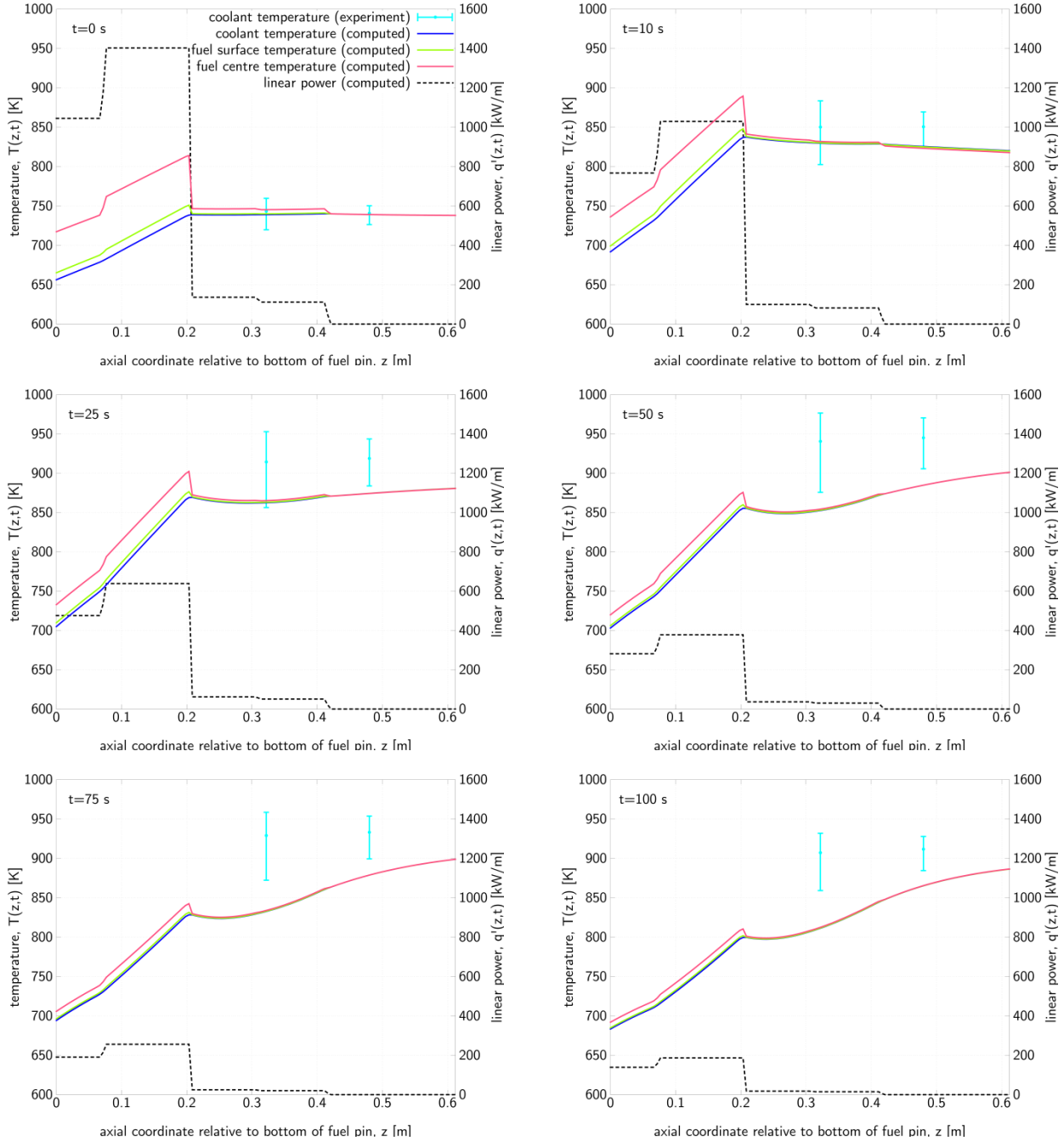


Figure 14. Axial distribution of fuel centreline temperature, fuel surface temperature, coolant temperature and linear power (averaged over the heated pins) at various times of the XX09 instrumented subassembly; for locations, see Figure 3, Figure 5 and Figure 6. The experimental band of the measured coolant temperature covers the values between the minimum and the maximum temperatures measured at the specified axial location.

6 Conclusions and perspective

The modelling approach and the results of the full-core neutronic/thermal-hydraulic analysis of the EBR-II SHRT-45R transient computed using the FRENETIC code are presented. Both the steady-state results and the transient results demonstrate the capability of the code to correctly describe those principal aspects of the physics that are important in the modelling of liquid-metal-cooled fast reactors, following the trend of the measured quantities. Discrepancies can be justifiably attributed both to the modelling assumptions and/or to the absence of models of certain physical phenomena which in this specific case appear to be of importance. As such, the study, development and implementation of additional physics models is foreseen.

7 Acknowledgements

This work is partially financially supported by the Italian “Ministero dello Sviluppo Economico”.

Participation in the CRP on the EBR-II SHRTs is under a research agreement between the Politecnico di Torino and the IAEA, CRP number I31021.

References

- [1] R. Bonifetto, S. Dulla, P. Ravetto, L. Savoldi Richard and R. Zanino, “A full-core coupled neutronic/thermal-hydraulic code for the modeling of lead-cooled nuclear fast reactors,” *Nuclear Engineering and Design*, vol. 261, pp. 85-94, 2013.
- [2] L. Briggs, T. Sumner, T. Fei, T. Sofu and S. Monti, “EBR-II passive safety demonstration tests benchmark analyses - phase 1,” in *2014 ANS Winter Meeting and Nuclear Technology Expo*, Anaheim, California, USA, 2014.
- [3] L. Briggs, S. Monti, W. Hu, D. Sui, G. H. Su, L. Maas, B. Vezzoni, U. Partha Sarathy, A. Del Nevo, A. Petruzzi, R. Zanino, H. Ohira, H. Mochizuki, K. Morita, C. Choi, A. Shin, M. Stempniewicz, N. Rtishchev, Y. Zhang and B. Truong, “EBR-II passive safety demonstration tests benchmark analyses - phase 2,” in *16th International Topical Meeting on Nuclear Reactor Thermalhydraulics*, Chicago, Illinois, USA, 2015.
- [4] A. Henry, *Nuclear-reactor analysis*, Cambridge, Massachusetts, USA: MIT Press, 1975.
- [5] R. Bonifetto, D. Caron, S. Dulla, P. Ravetto, L. Savoldi Richard and R. Zanino, *Extension of the FRENETIC code capabilities to the three-dimensional coupled dynamic simulation of LFR*, Madrid (Spain): Presented at the 16th International Conference on Emerging Nuclear Energy Systems (ICENES), 26-30 May, 2013.
- [6] D. Caron, S. Dulla and P. Ravetto, “New aspects in the implementation of the quasi-static method for the solution of neutron diffusion problems in the framework of a nodal method,” *Annals of Nuclear Energy*, vol. 87, pp. 34-48, 2016.
- [7] N. Todreas and M. Kazimi, *Nuclear systems*, New York, New York, USA: Hemisphere, 1990.
- [8] R. Zanino, R. Bonifetto, A. Ciampichetti, I. Di Piazza, L. Savoldi Richard and M. Tarantino, “First Validation of the FRENETIC Code Thermal-Hydraulic Model against the ENEA Integral Circulation Experiment,” *Transactions of the American Nuclear Society*, vol. 107, pp. 1395-1398, 2012.

- [9] R. Zanino, R. Bonifetto, A. Del Nevo and L. Savoldi, "Benchmark and preliminary validation of the thermal-hydraulic module of the FRENETIC code against EBR-II data," *Proceedings of the International Topical Meeting on Advances in Thermal Hydraulics (ATH)*, Reno, Nevada, 15-19 June 2014, pp. 173-187, 2014.
- [10] International Atomic Energy Agency, "Fast reactor database 2006 update, IAEA-TECDOC-1531," Vienna, 2006.
- [11] T. Sumner and T. Wei, "Benchmark Specifications and Data Requirements for EBR II Shutdown Heat Removal Tests SHRT-17 and SHRT-45R, ANL-ARC-226 (Rev 1)," Nuclear Engineering Division, Argonne National Laboratory, 2012.
- [12] T. Fei, A. Mohamed and T. Kim, "Neutronics Benchmark Specifications for EBR-II Shutdown Heat Removal Test SHRT-45R – Revision 1, ANL-ARC-228 (Rev 1)," Nuclear Engineering Division, Argonne National Laboratory, 2013.
- [13] J. Leppänen, *Development of a new Monte Carlo reactor physics code*, PhD Thesis, VTT Technical Research Centre of Finland, 2007.
- [14] M. Kellett, O. Bersillon and R. Mills, "The JEFF-3.1/-3.1.1 radioactive decay data and fission yields sub-libraries (JEFF report 20)," Nuclear Energy Agency, Paris, 2009.
- [15] A. Santamarina, D. Bernard, P. Blaise, M. Coste, A. Courcelle, T. Huynh, C. Jouanne, P. Leconte, O. Litaize, S. Mengelle, G. Noguère, J.-M. Ruggiéri, O. Sérot, J. Jommasi, C. Vaglio and J.-F. Vidal, "The JEFF-3.1.1 nuclear data library (JEFF report 22)," Nuclear Energy Agency, Paris, 2009.
- [16] G. Buckel and K. Kufner, "A fast reactor benchmark problem in two and three space dimensions, NEA/NEACRP/L(1976)167," Nuclear Energy Agency, Paris, 1976.
- [17] J. Fink and L. Leibowitz, "Thermodynamic and Transport Properties of Sodium Liquid and Vapor, ANL/RE-95/2," Argonne National Laboratory, 1995.
- [18] W. Rhoades and F. Mynatt, "DOT III two-dimensional discrete ordinates transport code, ORNL-TM-4280," Oak Ridge National Laboratory, Oak Ridge, Tennessee, USA, 1973.
- [19] H. Saller, R. Dickerson, A. Bauer and N. Daniel, "Properties of a fissium-type alloy, BMI-1123," Battelle Memorial Institute, Columbus, Ohio, USA, 1956.
- [20] T. Bauer, A. Wright, W. Robinson, J. Holland and E. Rhodes, "Behavior of modern metallic fuel in TREAT transient overpower tests," *Nuclear Technology*, vol. 92, no. 3, pp. 325-352, 1990.

Table 1. Energy structure adopted for the few-group cross sections of the EBR-II.

Group, g	Upper energy, E_{g-1} [MeV]	Lower energy, E_g [MeV]
1	—	4.0e-01
2	4.0e-01	6.0e-02
3	6.0e-02	1.0e-02
4	1.0e-02	1.5e-03
5	1.5e-03	2.5e-04
6	2.5e-04	0.0e+00

Table 2. Computed values of the effective delayed neutron precursors fractions by family.

Delayed neutron precursor family, i	Decay constant, λ_i [s⁻¹]	Effective delayed neutron fraction, $\beta_{eff,i}$ [pcm]
1	0.012467	22
2	0.028292	106
3	0.042524	67
4	0.133042	140
5	0.292467	226
6	0.666488	77
7	1.634780	67
8	3.554600	24

Table 3. Comparison of results between the predictor-corrector quasi-static and the point-kinetic methods: Δt_ϕ : shape time step; Δt_p : reactivity time step; t : time; $p(t)$: total power; $\rho(t)$: net reactivity; $T_{c,max}(t)$: peak coolant temperature; $T_{s,max}(t)$: peak fuel surface temperature; $T_{f,max}(t)$: peak fuel centreline temperature.

predictor-corrector quasi-static ($\Delta t_\phi=1\cdot10^{-3}$ s, $\Delta t_p=1\cdot10^{-3}$ s)						point-kinetic ($\Delta t_p=5\cdot10^{-3}$ s)				
t [s]	$p(t)$ [W]	$\rho(t)$ [pcm]	$T_{c,max}(t)$ [K]	$T_{s,max}(t)$ [K]	$T_{f,max}(t)$ [K]	$p(t)$ [W]	$\rho(t)$ [pcm]	$T_{c,max}(t)$ [K]	$T_{s,max}(t)$ [K]	$T_{f,max}(t)$ [K]
0.00e+00	6.000e+07	+0.000e+00	751.6	760.2	814.1	6.000e+07	+0.000e+00	751.6	760.2	814.1
1.00e-01	6.000e+07	+5.263e-02	751.6	760.2	814.1	6.000e+07	+5.272e-02	751.6	760.2	814.1
1.00e+00	5.987e+07	-1.449e+00	753.3	761.8	814.9	5.987e+07	-1.450e+00	753.3	761.9	814.9
1.00e+01	4.406e+07	-1.289e+02	877.9	885.1	915.7	4.404e+07	-1.290e+02	878.0	885.1	915.8
5.00e+01	1.619e+07	-2.592e+02	966.2	968.4	979.2	1.618e+07	-2.593e+02	966.0	968.2	979.0